



DYNAMICALLY PROPAGATING SHEAR BANDS IN IMPACT-LOADED PRENOTCHED PLATES—II. NUMERICAL SIMULATIONS

M. ZHOU,[†] G. RAVICHANDRAN[‡] and A. J. ROSAKIS[‡]

[†] George W. Woodruff School of Mechanical Engineering, Georgia Institute of Technology, Atlanta, GA 30332-0405, U.S.A.; and [‡] Graduate Aeronautical Laboratories, California Institute of Technology, Pasadena, CA 91125, U.S.A.

(Received 24 April 1995)

ABSTRACT

The experimental observations of dynamic failure in the form of propagating shear bands and of the transition in failure mode presented in Part I of this investigation is analyzed. Finite element simulations are carried out for the initiation and propagation of shear-dominated failure in prenotched plates subjected to asymmetric impact loading. Coupled thermomechanical simulations are carried out under the assumption of plane strain. The simulations take into account finite deformations, inertia, heat conduction, thermal softening, strain hardening and strain-rate hardening. The propagation of shear bands is assumed to be governed by a critical plastic strain criterion. The results demonstrate a strong dependence of band propagation speed on impact velocity, in accordance with experimental observations. The calculations reveal an active plastic zone in front of the tip of the propagating shear bands. The size of this zone and the level of the shear stresses inside it do not change significantly with the impact velocity or the speed of shear band propagation. Shear stresses are uniform inside this zone except near the band tip where higher rates of strain prevail. The shear band behind the propagating tip exhibits highly localized deformations and intense heating. Temperature rises are relatively small in the active plastic zone compared with those inside the well-developed shear band behind the propagating tip. The calculations also show shear band speeds and temperature rises that are in good agreement with experimental observations. Computed temperature fields confirm the experimental observation that dissipation continues behind the propagating shear band tip. In addition, the numerical results capture the arrest of the shear band. The arrested shear band is first subjected to reverse shear. Subsequently, the arrested band is subjected to mixed-mode loading which eventually leads to tensile failure at an angle about 30° to the band. Copyright © 1996 Elsevier Science Ltd

1. INTRODUCTION

Recent experiments have shown that structural metals are susceptible to failure in the forms of both propagating shear bands and/or propagating cracks when they are subjected to dynamic mode-II type of loading, Kalthoff (1987), Kalthoff and Winkler (1987), Mason *et al.* (1994a), and Zhou *et al.* (1996). Kalthoff (1987) and Kalthoff and Winkler (1987) found that loading rate can play a significant role in determining the activation of either the dynamic shear banding or the dynamic cracking mode of failure. In addition, Mason *et al.* (1994a) reported both modes of failure (shear banding and cracking) in one specimen and suggested that this transition can also result from changes in loading conditions. Zhou *et al.* (1996) found that this transition

exists in a high strength maraging steel (C-300) but not in a titanium alloy (Ti-6Al-4V), demonstrating that the transition is also material dependent. While the time-dependent nature of dynamic loading makes evolution in loading history inevitable, it is possible to prevent or induce either or both shear banding and cracking by the selection of materials based on their properties and resistances to these two forms of failure. To achieve this, it is necessary to understand the mechanisms and conditions through which these two forms of failure occur and interchange. Indeed, it has been theorized that at higher loading rates enhanced thermal softening suppresses the brittle failure that occurs at lower rates of loading and provides a mechanism for a more "ductile" shear mode of failure—propagating shear bands, see Lee and Freund (1990), and Needleman and Tvergaard (1994). This selection of failure modes is an important issue because it concerns the failure of materials in real engineering applications. Such applications include high speed machining (Gioia and Ortiz, 1996), penetration (Hanchak *et al.* 1993, Magness, 1994) and materials processing (Nesterenko *et al.*, 1994).

Unlike the dynamic propagation of cracks, the propagation of shear bands has not been widely studied. An approximate analysis of propagating shear bands was conducted by Grady (1992). Gioia and Ortiz (1996) analytically studied the two-dimensional structure of propagating shear bands in thermoviscoplastic solids using a boundary layer theory. Mason *et al.* (1994a) studied the deformation fields around propagating shear bands and interpreted the results using a mode-II Dugdale model. The experimental investigation of Zhou *et al.* (1996) revealed the dependence of temperature inside the propagating shear bands on impact speed (loading rate) and studied the characteristics of the temperature fields generated by these bands. The highest temperature observed in C-300 steel approaches 90% of its melting point. On the other hand, optical measurements demonstrated the histories of shear band propagation speed and their strong dependence on impact velocity. Additionally, the process of failure mode transition from shear banding to fracture was also recorded for specimens of C-300 steel.

The analysis presented here concerns the initiation and propagation of shear bands and the transition of failure mode from shear banding to fracture as observed in the experiments of Zhou *et al.* (1996). This paper comprises the second part of a combined experimental and numerical effort that is directed at gaining insight into these phenomena. The model material is the C-300 steel used in the experiments. The objective is to achieve better understanding of the complex phenomena observed in the experiments through finite element simulations using the actual specimen geometry. The simulations account for the dynamic nature of the phenomenon including elastic-thermoplastic finite deformations, rate sensitivity, strain hardening, thermal softening and the full coupling of mechanical deformation and heat conduction. In the simulations, the initiation and propagation of shear failure are assumed to be controlled by a critical strain criterion; and the initiation and propagation of tensile fracture are assumed to be controlled by a critical stress criterion. The numerical analysis is a full-scale simulation taking into account the boundary and initial conditions of the experiments. The boundary conditions are as they occur in the experiments. Most material constitutive parameters are measured through independent split Hopkinson (Kolsky) bar experiments over a wide range of strain rate.

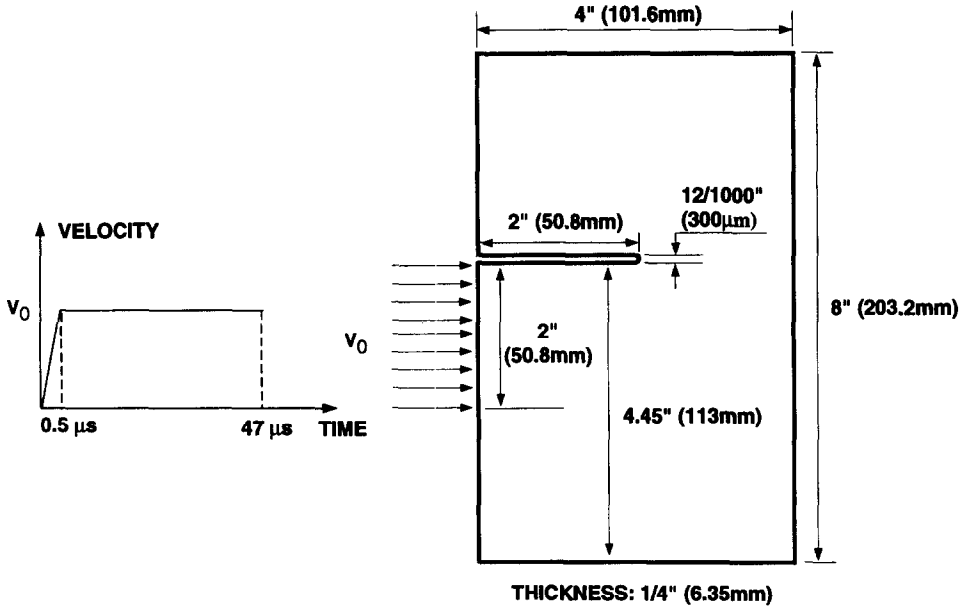


Fig. 1. Asymmetric impact configuration analyzed.

2. PROBLEM ANALYZED

The configuration analyzed here and the observed failure modes are shown in Fig. 1 in the experimental part (Part I) of this series (see Zhou *et al.*, 1996). This configuration allows the notch tip region of the specimen to be loaded in mode-II through the asymmetric impact. For C-300 steel, both shear banding and cracking may be observed depending on the impact velocity. A shear band initiates from the notch tip when the impact velocity V_0 is greater than approximately 20 ms^{-1} . The shear band propagates in a direction nearly parallel to the direction of impact, with a slight tilt toward the side of impact (lower side in Fig. 1). When V_0 is also below a critical value (approximately 29 ms^{-1} , $20 \text{ ms}^{-1} < V_0 < 29 \text{ ms}^{-1}$), the band eventually arrests inside the specimen and a crack extends from the tip of the shear band in a direction approximately 30° to the direction of impact. When V_0 is greater than 29 ms^{-1} , the shear band propagates throughout the whole ligament and no crack is observed.

The analysis discussed here concerns the full scale simulation of the deformation in a specimen whose geometry is shown in Fig. 1. The impact loading is simulated by a velocity boundary condition over the width where the projectile comes into contact with the specimen. Impact velocities between 20 and 30 ms^{-1} are of primary interest. This is an impact velocity range over which both types of failure and the failure mode transition are observed. The velocity boundary condition is also illustrated in Fig. 1. The imposed velocity increases linearly from zero to a constant value over $0.5 \mu\text{s}$. This ramp accounts for the initiation of contact between the projectile and the specimen that may not be instantaneous. The constant boundary velocity is imposed for up to $47 \mu\text{s}$ after impact, after which the surface is assumed to be traction-free.

This models the separation of the projectile from the specimen resulting from wave reflections within the projectile and the specimen. The specimen is initially stationary. All surface areas have traction free boundary conditions except where the velocity boundary condition is applied. Under this type of impact loading, the notch faces may close (Lee and Freund, 1990). Contact forces are applied to prevent interpenetration in the calculation when closure of the notch faces occurs. Numerically, this is implemented by activating tractions that increase with decreasing notch surface gap according to a preassumed constitutive equation when the separation is sufficiently small (e.g. within 1 μm).

3. NUMERICAL FORMULATION

Finite element simulations described here are based on a finite deformation formulation of LeMonds and Needleman (1986), Needleman (1989), and Needleman and Tvergaard (1991). The simulation considers the full coupling between the thermal and mechanical processes of dynamic deformation.

3.1. Governing equations

The coupled system of field equations are the dynamic principle of virtual work which specifies balance of momentum

$$\int_V \boldsymbol{\tau} \cdot \delta \mathbf{E} dV = \int_S \mathbf{t} \cdot \delta \mathbf{u} dS - \int_V \rho \frac{\partial^2 \mathbf{u}}{\partial t^2} \cdot \delta \mathbf{u} dV, \quad (1)$$

and the variational form of heat equation which specifies balance of energy

$$\int_V \rho c_p \dot{T} \delta T dV = \int_V \chi \boldsymbol{\tau} \cdot \mathbf{D}^p \delta T dV + \int_S k(\mathbf{F}^{-1} \mathbf{F}^{-T} \nabla T) \cdot \mathbf{N} \delta T dS - \int_V k(\mathbf{F}^{-1} \mathbf{F}^{-T} \nabla T) \cdot \nabla \delta T dV. \quad (2)$$

In the above equations, V and S represent, respectively, the volume and surface of a body in the reference configuration, $\boldsymbol{\tau} = J\boldsymbol{\sigma} = \det|\mathbf{F}|\boldsymbol{\sigma}$ is the Kirchoff stress, with $\boldsymbol{\sigma}$ the Cauchy stress, and \mathbf{F} is the deformation gradient. \mathbf{t} is the traction on a surface with normal \mathbf{N} in the reference configuration, \mathbf{u} is the displacement, \mathbf{E} denotes the Lagrangian strain, t is time, ρ is mass density in the reference configuration, T is temperature, χ denotes the fraction of plastic work converted to heat, \mathbf{D}^p is the plastic part of the rate of deformation, c_p is specific heat, k is heat conductivity, (\cdot) denotes $\partial/\partial t$, ∇ denotes gradient in the reference configuration, $(\cdot)^{-1}$ and $(\cdot)^{-T}$ denote, respectively, inverse and inverse transpose, δT , $\delta \mathbf{E}$ and $\delta \mathbf{u}$ denote admissible variations in temperature, Lagrangian strain and displacement, respectively.

Table 1. *Material parameters for C-300 steel*

Parameter	Value
$\dot{\epsilon}_0$	$1 \times 10^{-3} \text{ s}^{-1}$
m	70
σ_0	2000 MPa
ϵ_0	σ_0/E
n	0.01
T_0	293 K
δ	0.8
κ	500 K
E	200 GPa
ν	0.3
ρ	7830 kg m^{-3}
c_p	$448 \text{ J}(\text{kg} \cdot \text{K})^{-1}$
k	$34.6 \text{ W}(\text{m} \cdot \text{K})^{-1}$
α	$11.2 \times 10^{-6} \text{ K}^{-1}$
χ	0.9

3.2. Constitutive relations

The constitutive relation is written as (Povirk *et al.*, 1993)

$$\dot{\boldsymbol{\tau}} = \mathbf{L} \cdot [\mathbf{D} - \mathbf{D}^p - \alpha \dot{T} \mathbf{I}], \quad (3)$$

where $\dot{\boldsymbol{\tau}}$ is the Jaumann rate of Kirchhoff stress, \mathbf{L} is the tensor of elastic moduli, \mathbf{D} is the rate of deformation tensor, α is the coefficient of thermal expansion, and \mathbf{I} is the second order identity tensor. For an isotropically hardening, viscoplastic solid $\mathbf{D}^p = (3\dot{\bar{\epsilon}}/2\bar{\sigma})\boldsymbol{\tau}'$, with $\dot{\bar{\epsilon}}$ being the equivalent plastic strain rate, $\boldsymbol{\tau}' = \boldsymbol{\tau} - \frac{1}{3}(\boldsymbol{\tau} \cdot \mathbf{I})\mathbf{I}$ and $\bar{\sigma} = \frac{3}{2}\boldsymbol{\tau}' \cdot \boldsymbol{\tau}'$.

The viscoplastic response of the material for the strain-rate range of 10^{-3} s^{-1} to $1 \times 10^4 \text{ s}^{-1}$ is characterized by the following equations

$$\left. \begin{aligned} \dot{\bar{\epsilon}} &= \dot{\epsilon}_0 \left[\frac{\bar{\sigma}}{g(\bar{\epsilon}, T)} \right]^m, \\ g(\bar{\epsilon}, T) &= \sigma_0 (1 + \bar{\epsilon}/\epsilon_0)^n \left\{ 1 - \delta \left[\exp\left(\frac{T - T_0}{\kappa}\right) - 1 \right] \right\}, \end{aligned} \right\} \quad (4)$$

where $\bar{\epsilon} = \int_0^t \dot{\bar{\epsilon}} dt$ is the equivalent plastic strain, $\dot{\epsilon}_0$ is a reference strain rate, m is a rate sensitivity parameter, σ_0 is the yield stress, $\epsilon_0 = \sigma_0/E$ is a reference strain rate, n is the strain hardening exponent, T_0 is a reference temperature, and δ and κ are thermal softening parameters. The function $g(\bar{\epsilon}, T)$ represents the stress-strain relation at the quasi-static strain rate of $\dot{\epsilon}_0$ and at temperature T . At $T = T_0$, $g(\bar{\epsilon}, T) = \sigma_0(1 + \bar{\epsilon}/\epsilon_0)^n$. Most of these constitutive law parameters are measured using split Hopkinson bar experiments conducted over a range of strain rates. Values of the parameters used in the simulations are listed in Table 1 and correspond to C-300 steel, see, e.g. Mason *et al.* (1994a).

3.3. Failure criteria

In addition to thermal softening, localized deformations are also accompanied by material weakening due to the formation of microvoids. The extensive damage and failure through void initiation, growth and coalescence observed inside the shear bands in experiments (Zhou *et al.*, 1996) attest to the important role of such weakening mechanisms in the initiation and propagation of shear bands in this material. In the present paper, the process of void development is not explicitly simulated. Rather, the material weakening is modelled by the use of a failure criterion and a constitutive characterization that specifies lower stress-carrying capabilities for damaged materials. Specifically, ductile failure is assumed to initiate when the equivalent plastic strain reaches a certain critical value. The failure condition is given by

$$\bar{\varepsilon}_c = \varepsilon_1 + (\varepsilon_2 - \varepsilon_1) \frac{\dot{\varepsilon}_r}{(\dot{\varepsilon}_r + \dot{\bar{\varepsilon}})}, \quad (5)$$

where ε_1 and ε_2 are, respectively, the critical strains at which the material is assumed to lose significantly its stress-carrying capability as $\dot{\bar{\varepsilon}} \rightarrow \infty$ and at $\dot{\bar{\varepsilon}} = \dot{\varepsilon}_0$. Also, $\dot{\varepsilon}_r$ is a rate-dependence parameter. The motivation to choose such a rate-dependent form for the critical strain is the experimental observation that at higher strain rates deformations localize and materials fail at lower levels of plastic strains. Such a simple criterion may not capture all the complicated features of the failure occurring inside the shear bands. Rather, it is a phenomenological characterization that allows the initiation and propagation of shear bands to be studied under a relatively simple theoretical framework. Once the critical strain $\bar{\varepsilon}_c$ is reached (5), the damaged material is modelled to behave like a viscous fluid. Specifically, the stress-carrying capability by the material is assumed to follow that of a Newtonian fluid, carrying both a hydrostatic pressure component and a viscous stress component, i.e.

$$\boldsymbol{\tau} = - \frac{\gamma[1 - J + \alpha(T - T_0)]}{J} \frac{E}{1 - \nu} \mathbf{I} + \mu \mathbf{D}, \quad (6)$$

where γ is a stiffness parameter and μ is the viscosity. The use of such a constitutive relation for material inside the shear band is motivated by their ability to sustain pressure, by the continued dissipation through deformation and frictional forces and by the high temperature values observed in the experiments as discussed in Zhou *et al.* (1996).

The above critical strain criterion is appropriate in describing shear-dominated ductile failure. In order to account for the possibility of other mechanisms of material decohesion, e.g. tensile failure, we introduce the following additional failure condition. Tensile failure is assumed to occur when the maximum tensile stress exceeds a certain value, or

$$\sigma_{\max} \geq \sigma_{\text{cr}}, \quad (7)$$

where σ_{cr} is a critical threshold stress for failure. It is taken to be equal to three times the yield stress to account for the effect of high triaxiality which is expected to dominate at the tip of an initiating crack in a ductile solid. The material is assumed

Table 2. *Damage model parameters*

Parameter	Value
ε_1	$4\sigma_0/E$
ε_2	0.3
$\dot{\varepsilon}_r$	$4 \times 10^4 \text{ s}^{-1}$
Υ	0.002
μ	$5 \times 10^{-4} \text{ MPa s}$
σ_{cr}	$3\sigma_0$

to have no tensile stress-carrying capability after either criterion [(5) or (7)] is satisfied. Specifically in the analysis, the hydrostatic component of the stress is non-positive or $\tau \cdot \mathbf{I} \leq 0$ for failed material elements. The relevant material parameters in (5)–(7) appear in Table 2.

The use of the above failure criteria allows the initiation and propagation of shear bands and the evolution and transition of failure modes to be simulated. Also, the effects of various factors, such as impact velocity and different combinations of material properties, can be explored.

3.4. *Finite element method*

When the finite element approximations of the displacement and temperature fields are substituted into the momentum balance (1) and the energy balance (2), the resulting equations take the form

$$\mathbf{M} \frac{\partial^2 \mathbf{U}}{\partial t^2} = \mathbf{R}, \quad (8)$$

and

$$\mathbf{C} \frac{\partial \mathbf{T}}{\partial t} = -\mathbf{K}\mathbf{T} + \mathbf{H}, \quad (9)$$

where \mathbf{U} is the vector of nodal displacements, \mathbf{T} is the vector of nodal temperatures, \mathbf{M} , \mathbf{C} and \mathbf{K} are the mass, the heat capacitance and the heat conductance matrices, and \mathbf{R} and \mathbf{H} are the mechanical and thermal force vectors, respectively.

A lumped mass matrix is used in (8), for reasons of efficiency and accuracy, Krieg and Key (1973). Equation (8) is integrated using the Newmark β -method, with $\beta = 0$ and $\gamma = 0.5$, Belytschko and Chiapetta, (1976). The integration of (9) using a lumped heat capacitance matrix and the numerical scheme for solving the coupled system of (8) and (9) are discussed in Zhou *et al.* (1994).

4. RESULTS AND DISCUSSION

4.1. *Initiation and propagation of shear bands and failure mode transition*

Full-scale finite element simulations of the experiments are conducted using a two-dimensional, plane strain model. The experimental observation of shear band surfaces

with uniform deformations across specimen thickness (see Fig. 3 of Part I) motivates the use of a two-dimensional plane strain model in this study. First, the initiation and propagation of shear band and the transition in failure mode as observed in experiments are considered. Since the evolution of failure is closely related to loading conditions in the specimen, contour plots are chosen to best summarize the state of stress at different stages during the course of the experiment. Shear-dominated states of stress are best characterized by contour plots of the shear component σ_{12} of the Cauchy stress in a fixed Cartesian frame while the opening-dominated states are best characterized by the hoop stress $\sigma_{\theta\theta}$ in a polar coordinate system centered at the tip of the propagating shear band.

Figure 2 shows a sequence of σ_{12} distributions at different times after impact. The impact velocity is 25 ms^{-1} . This is an intermediate velocity at which both shear banding and fracture are observed in the experiments, as illustrated in Fig. 1(a) of Part I. The distributions are shown for times between 24 and $145.6 \mu\text{s}$ after impact. Corresponding distributions of hoop stress $\sigma_{\theta\theta}$ in a coordinate system centered at the running tip of the shear band are shown in Fig. 3. The stress pulse generated by the impact first arrives at the notch tip region at about $10 \mu\text{s}$ after impact. The pulse causes shear loading to the tip as seen in Fig. 2(a–c). The existence of a severe shear stress state (mode-II conditions) is also reflected in the asymmetry in $\sigma_{\theta\theta}$ distributions in Fig. 3(a–c). This loading is responsible for the initiation and propagation of shear bands. The simulations show that the initiation of the shear band occurs at approximately $22 \mu\text{s}$. This initiation time corresponds to the activation of the critical strain criterion of (5). This is consistent with the initiation time observed in experiments at this impact velocity by Zhou *et al.* (1996). As the shear band propagates the size of the area in front of the band tip where intensive shear exists increases and reaches a maximum at approximately $44\text{--}45 \mu\text{s}$, see Fig. 2(c) and Fig. 3(c). The size of this area and the intensity of the shear stress inside it decrease gradually following this point. By $65 \mu\text{s}$, the shear mode of loading in the shear band tip region has ceased to exist, Fig. 2(d) and Fig. 3(d). As a result, the shear band decelerates and eventually arrests. Since the propagation of the shear band is directly related to the evolution of this shear mode of loading, the duration over which this shear loading exists is the duration of shear band propagation. In the calculations, this period is between 20 and $60 \mu\text{s}$. In the experiment, shear band propagation is observed to occur in the same time period, see Fig. 18 of Part I. The tip of the shear band is not subjected to intense loading between $65\text{--}80 \mu\text{s}$, Fig. 2(e) and Fig. 3(e). Following this period, a shear mode of loading in the opposite direction relative to the initial direction of shear develops, Fig. 2(f) and Fig. 3(f). The intensity of this shear mode of stresses is lower than that of the initial shear loading, as partly indicated by the smaller size of the area over which this mode of loading exists. No significant shear band extension occurs during this period.

After approximately $135 \mu\text{s}$, a tensile mode of loading exists in the specimen and the shear band starts to open up in a crack-like fashion, Fig. 2(g–h) and Fig. 3(g–h). This stress state intensifies and is accompanied by increases in the magnitude of tensile stresses at the tip of the arrested shear band. Figure 4 is a plot of the time history of the maximum tensile stress in the specimen. The increase in the tensile stress at $135 \mu\text{s}$ corresponds to the emergence of the tensile loading tip region seen in Fig. 3(g–h).

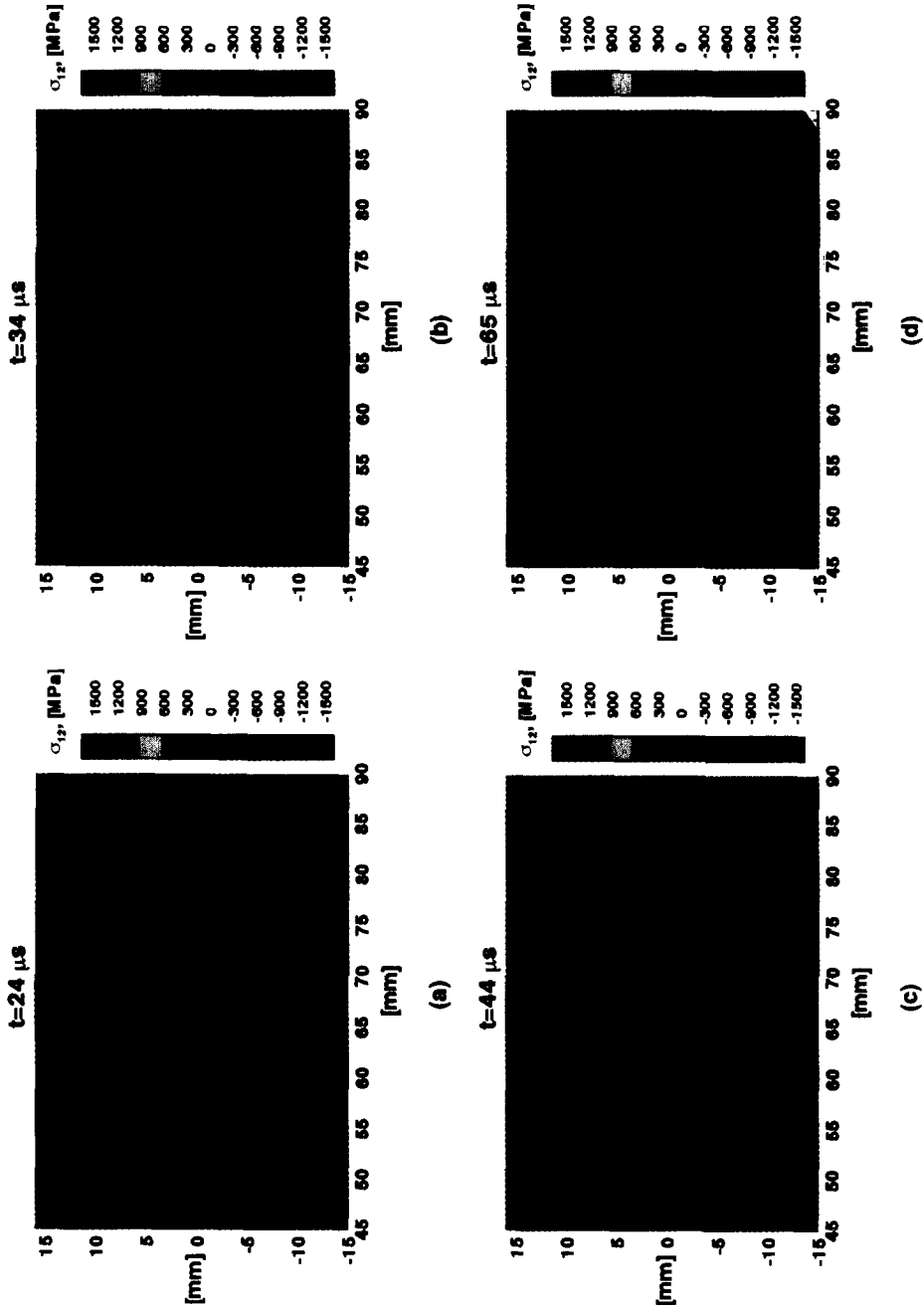
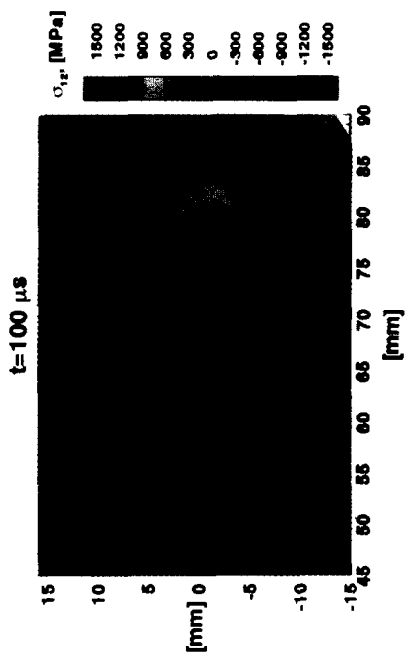
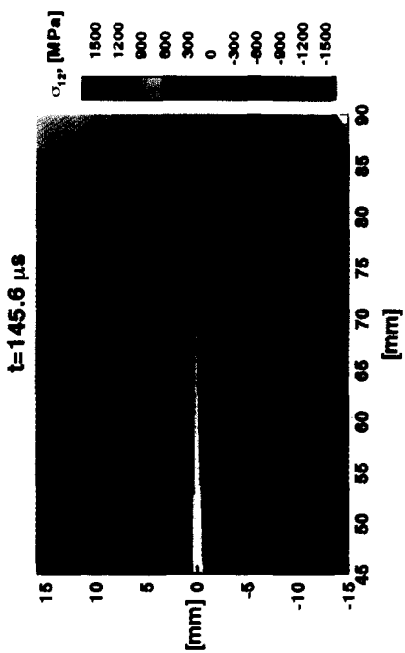


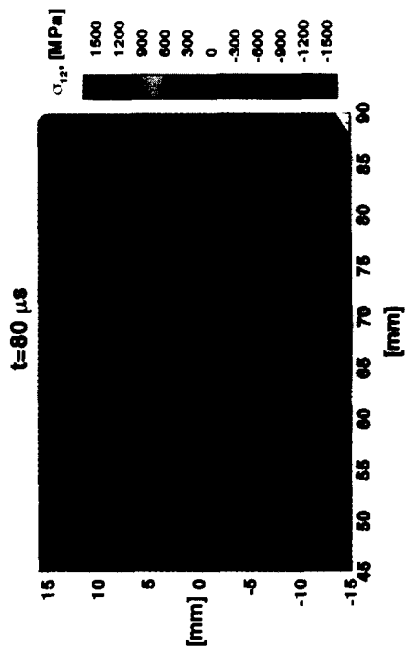
Fig. 2. Distributions of shear stress component σ_{12} at different times after impact. $V_0 = 25 \text{ ms}^{-1}$.



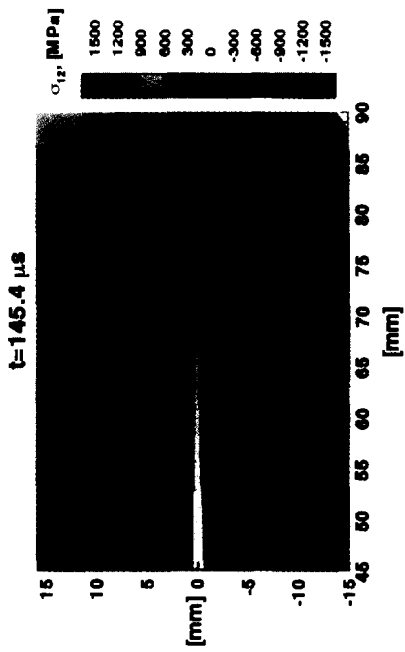
(f)



(h)



(e)



(g)

Fig. 2. (Continued).

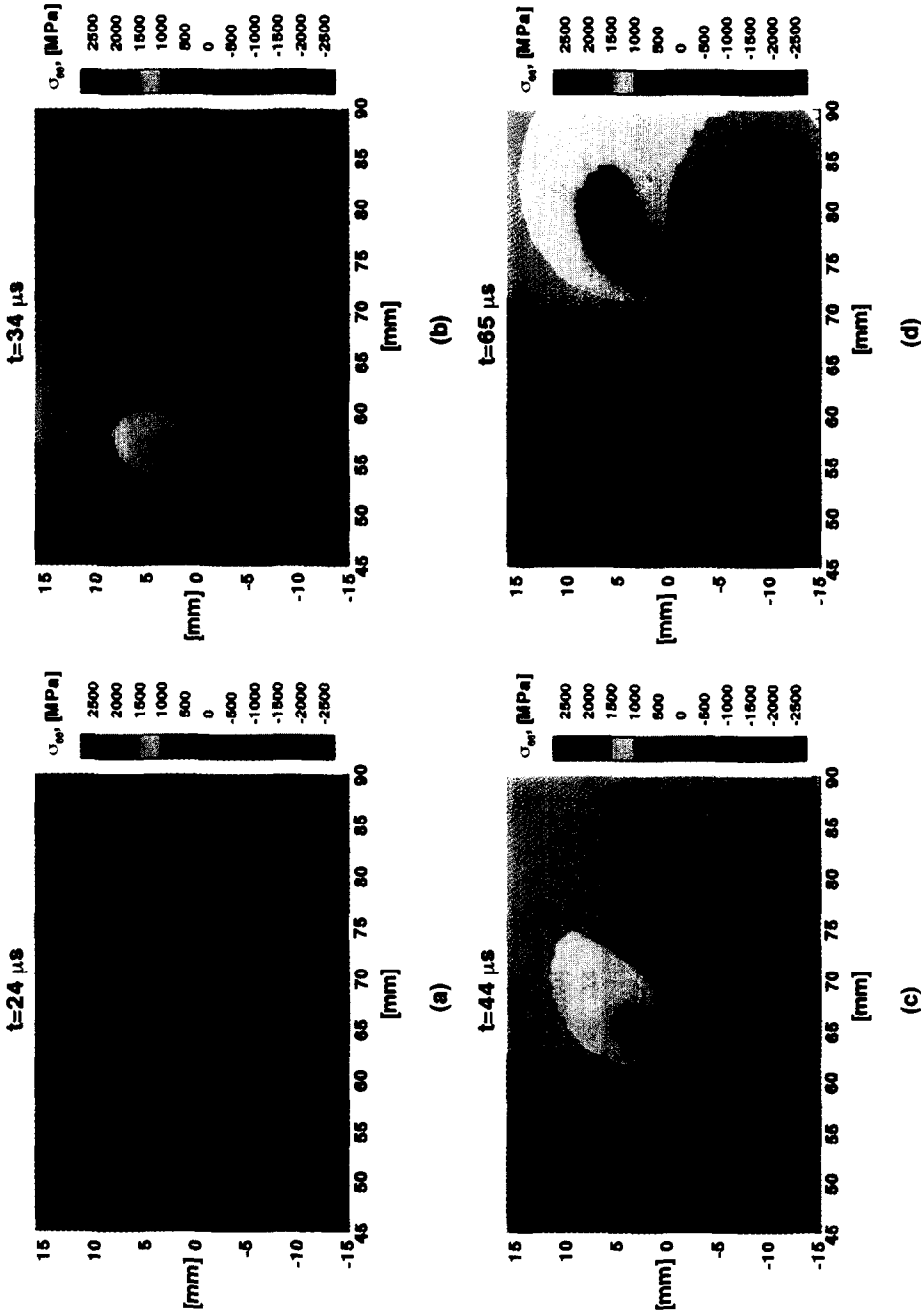


Fig. 3. Distributions of hoop stress σ_{θ} , at different times after impact, $V_0 = 25 \text{ ms}^{-1}$.

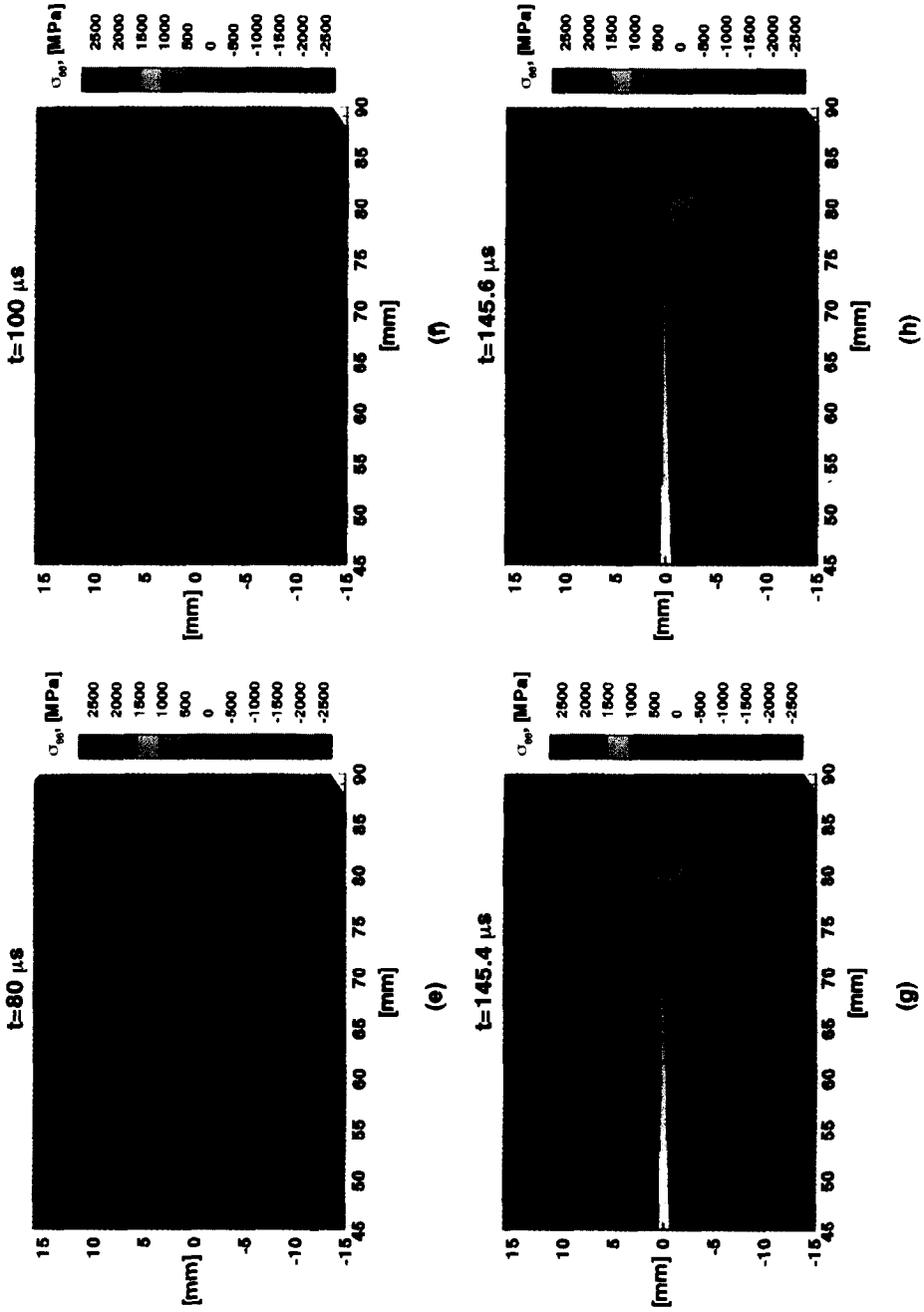


Fig. 3. (Continued).

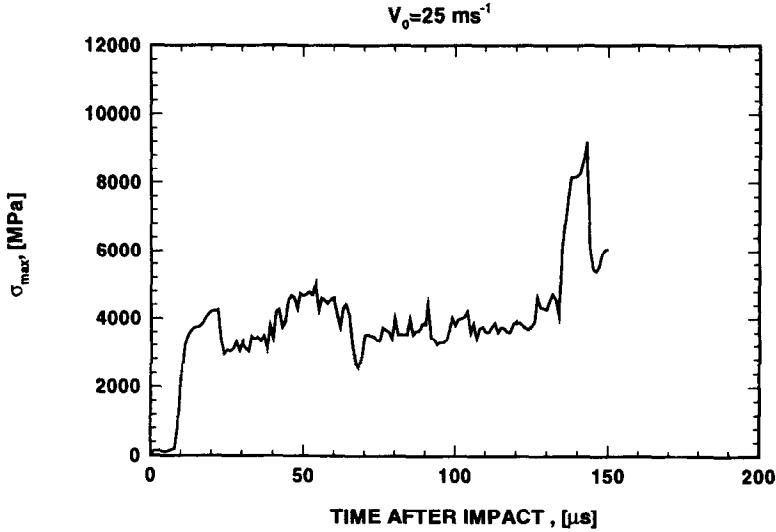


Fig. 4. History of maximum tensile stress in the specimen, $V_0 = 25 \text{ ms}^{-1}$.

A detailed image of this mode of loading in the tip region of the arrested shear band is shown in Fig. 5. A crack initiates and propagates from the shear band tip at approximately $145 \mu\text{s}$. The crack initiation time corresponds to the activation of the critical-stress failure condition of (7). This crack is oriented in a direction approximately 30° from the direction of initial impact, similar to what is observed in experiments, see Fig. 3 of Part I.

The results shown in Figs 2 and 3 illustrate the time sequence for the occurrence of the shear band and the crack. Furthermore, the results also demonstrate that while the transition of failure mode is related to material properties [such as the critical strain and critical stress for failure in (5) and (7)] it is also influenced by changes in loading characteristics. The results in Figs 2 and 3 are mainly used to demonstrate the occurrence of this transition. The use of (7) in the current context does not provide a realistic simulation of the crack speed as there is no physical length scale operative except the size of the mesh in the vicinity of the crack tip. However, the results clearly illustrate the emergence of the tensile mode of loading that is responsible for the resulting tensile failure. It should be pointed out that the speed of the shear band propagation as reflected in Figs 2 and 3 and discussed later is independent of the mesh size because the material does not lose all stress-carrying capability [see (6)] after the condition in (5) is satisfied. Some calculations are conducted with a mesh size that is one-half of that used in Figs 2 and 3. The resulting shear band speed is within 3% of what is discussed here.

Numerical simulation was also performed for an impact velocity of 30 ms^{-1} . This impact velocity is above the critical value of 29 ms^{-1} for which the shear band propagates throughout the whole ligament of the specimen in the experiment. In this simulation, the speed of shear band propagation is higher than that in Figs 2 and 3, consistent with what is observed in experiments. As a result of the higher speed of propagation, the band propagates out of the specimen by $60 \mu\text{s}$.

In the following section, we use the results of the numerical analysis to investigate detailed features of shear band initiation and growth.

4.2. Shear stress distributions in front of the shear band tip

The initiation, propagation and arrest of a shear band depend on the intensity of the shear stresses in the vicinity of the band tip. The intensity of this loading also affects the rate of deformation inside the band process zone and reflects the material resistance to the propagation of shear bands. Figure 6 summarizes the evolutions of shear stress σ_{12} along a line directly in front of the band tip for the two impact velocities discussed above. In Fig. 6(a), it can be seen that the shear stress is uniform over a distance of approximately 9 mm from the shear band tip. However, very near the tip the stress is higher because of the higher strain rates there. The size of this region of uniform stress is smaller initially (see, e.g. the curve for 20 μs). The size increases gradually and reaches a maximum at approximately 40 μs and remains at this maximum until 52 μs . In Fig. 6(b), the impact velocity is 30 ms^{-1} . Despite the higher impact velocity and the higher speed of shear band propagation the size of the area of intense shear stresses is still 8 mm, approximately the same as or slightly smaller than that in Fig. 6(a). In addition, the shear stresses are approximately 1450 MPa, the same as those in Fig. 6(a). This demonstrates that increased loading rate causes the shear band to propagate at higher speeds under approximately the same stress conditions in front of the band tip. Once the shear band initiates the material does not seem to be capable of sustaining higher levels of stresses in front of the shear band. These general features are consistent with the concepts proposed by Grady (1992, 1994) who introduced the idea of an active shear process zone at the tip of the propagating shear band. The level of the nearly constant shear stress observed in the simulations are also in excellent agreement with the results of the optical measurement reported by Mason *et al.* (1994a). In their measurements, a shear line plastic zone model was used to interpret optical CGS patterns and to infer the average value of the shear stress associated with the band growth.

During the propagation of the shear band, the shear stress distribution in front of the band tip is approximately symmetric in the direction perpendicular to the band, see Fig. 2(a–c). The shear stress is highest at the centerline of the shear band and decreases asymptotically away from it. These results are in good agreement with the boundary layer solution of Gioia and Ortiz (1996).

4.3. Temperature field around the shear bands

Since the propagation of shear bands is a coupled thermo-mechanical event, temperature increases and the resulting thermal softening play an important role in the evolution of failure. The computations reveal that there is significant temperature increase within 1 mm on both sides of the shear band as well as in front of its travelling tip. The increase is localized and is highest in a narrow band. An example of the temperature distribution corresponding to $t = 44 \mu\text{s}$ for an impact velocity of $V_0 = 25 \text{ms}^{-1}$ is shown in Fig. 7.

Propagating shear bands are different from one-dimensional shear bands in that deformation and temperature fields are non-uniform along the bands as well as across

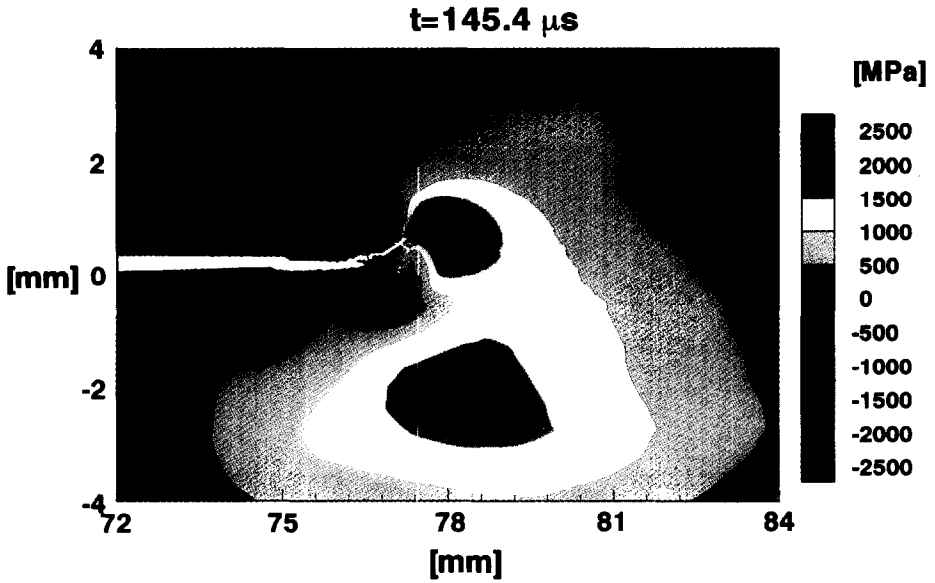


Fig. 5. Distribution of hoop stress $\sigma_{\theta\theta}$ around the propagating tip of a crack, $t = 145.4 \mu$ s.

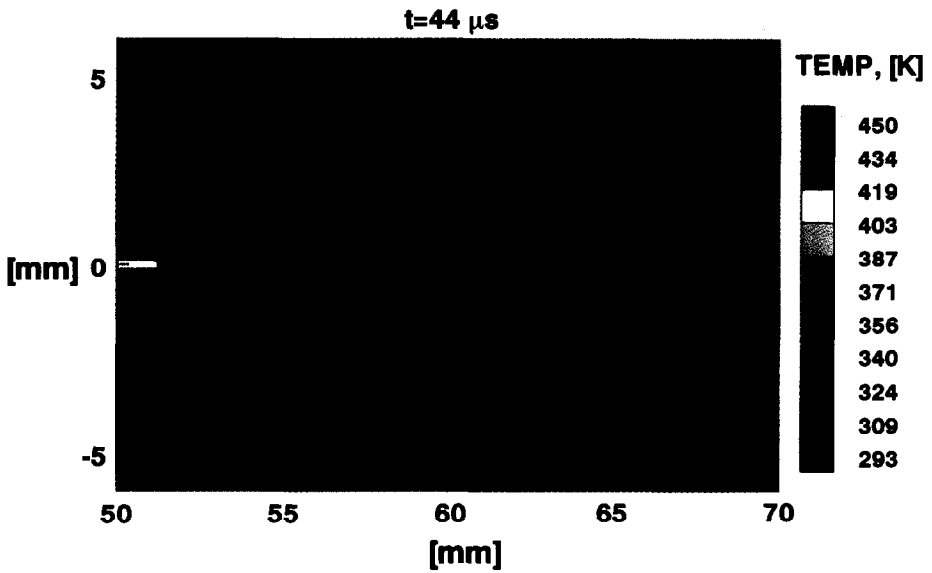


Fig. 7. Temperature field around a propagating shear band at 44μ s after impact, $V_0 = 25 \text{ ms}^{-1}$.

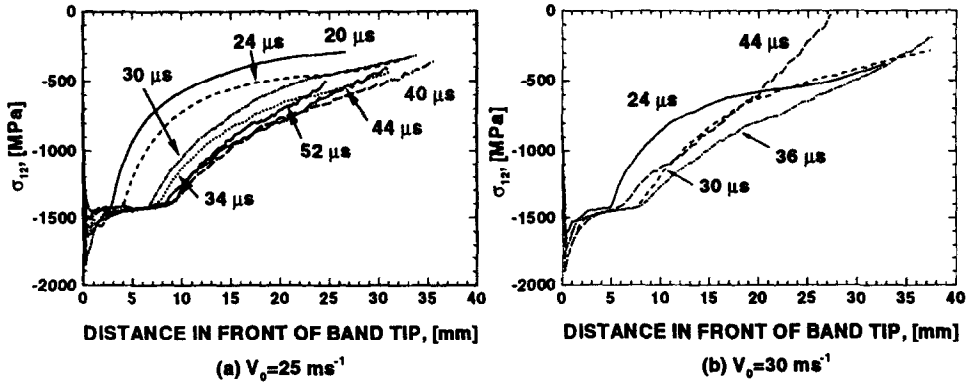


Fig. 6. Distributions of shear stress component σ_{12} in front of shear band tip at different times after impact for $V_0 = 25 \text{ ms}^{-1}$ and $V_0 = 30 \text{ ms}^{-1}$.

them. Because of the propagation, different parts of the bands are at different stages of deformation. Figure 8 shows the temperature variations along the center line of a shear band at different times after impact. First, note that the size of the zone of significant temperature rises in front of the tip is approximately 9 mm. This is also the size of the active plastic zone and the zone of nearly constant shear stresses in front of the tip, see Fig. 6. The maximum temperature rise inside the active plastic zone is on the order of 500 K. This temperature remains constant inside the plastic zone throughout propagation. Behind the tip, the temperature continues to increase, at slower rates, as the band propagates. Higher temperatures exist near the tip of the

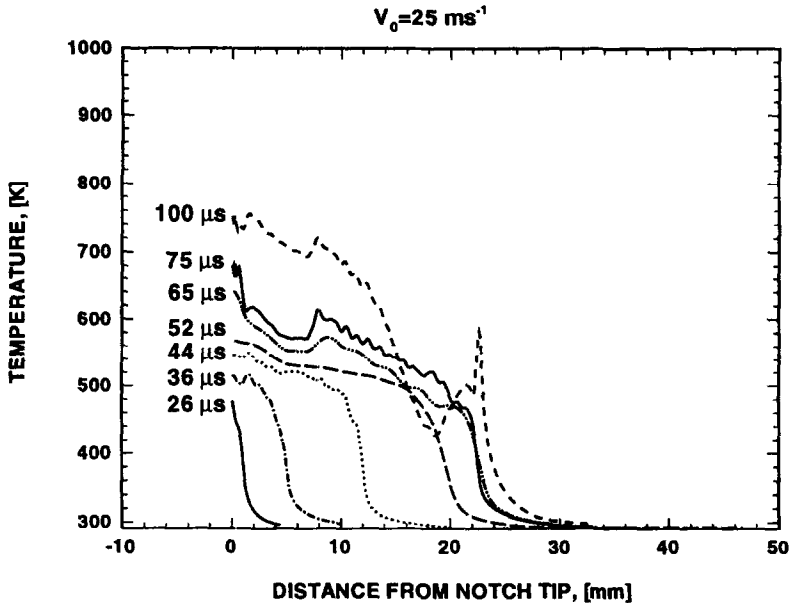


Fig. 8. Temperature profiles along shear band line at different times after impact, $V_0 = 25 \text{ ms}^{-1}$.

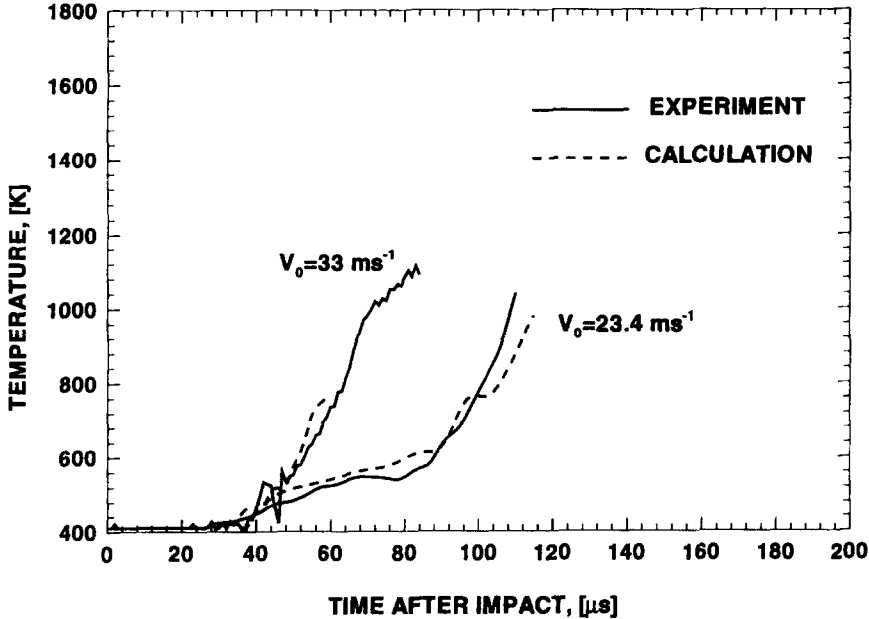


Fig. 9. Temperature increases at different impact velocities; (3 mm in front of notch tip, at center of shear band).

original notch where the amount of deformation is the highest partly due to longer durations of localized deformation there. This continued temperature increase behind the tip is in good agreement with the results of infrared measurements in Part I of this investigation, Zhou *et al.* (1996). The continued deformation and dissipation are in contrast to the propagation of cracks where the crack faces separate and no further deformation and dissipation occur behind the crack tip. In addition to the different kinetic nature of shear deformation in propagating shear bands (compared with that of propagating cracks, Zehnder and Rosakis, 1992), the presence of pressure in this impact configuration also contributes to the continued heat generation by prolonging the deformation before the eventual fracture of the material.

Figure 9 compares the calculated temperature profiles and the corresponding profiles measured in experiments. The profiles correspond to temperatures in the middle of the shear bands. They are obtained by focusing a detector at a point 3 mm in front of the notch tip before impact. For details, see Part I of this investigation. During the deformation the shear band tip propagates forward and passes through the point of observation. The temperature profiles discussed here are the temperature histories recorded by that detector. Each profile shown corresponds to a particular impact velocity. Temperature profiles at two impact velocities (25 and 30 ms^{-1}) are shown. Both the experimental profiles and the calculated profiles show relatively slow initial increases followed by quicker increases, consistent with the distribution shown in Figs 7 and 8. There is a good agreement between the experimental and the calculated curves. The curves show higher temperatures and higher rate of increase for higher impact velocities.

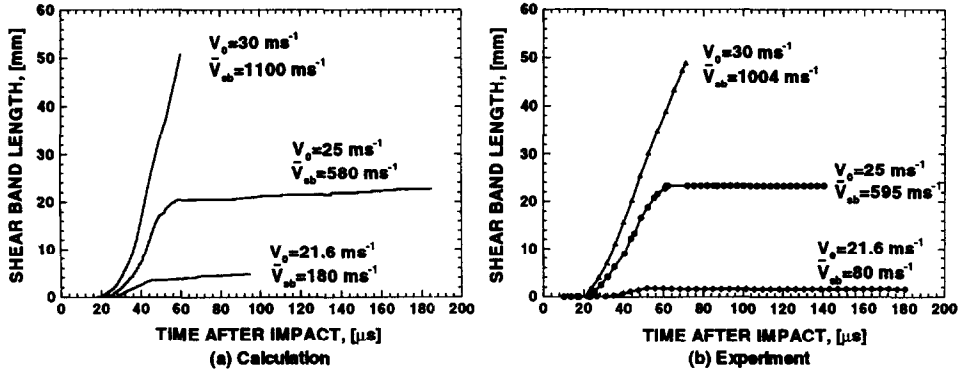


Fig. 10. Comparison of calculated and measured shear band lengths, (a) calculation, (b) experiment.

4.4. Shear band length histories and shear band speed

The length history of a propagating shear band contains information about its characteristics including the time of initiation, the time of arrest and the speed of propagation. Figure 10 is a summary of the calculated length histories of propagating shear bands at three impact velocities. The corresponding experimental results are also shown. Clearly, these two sets of results are in good agreement. The curves show a dramatic increase in the length and speed of shear band propagation with increasing impact velocity. In addition, the profiles indicate that the shear band speed is lower initially. It increases and reaches a maximum at approximately $45 \mu\text{s}$. This corresponds to the time of Fig. 2(c) when the size of the area of intense shear stress is maximum. The speed decreases after $45 \mu\text{s}$. While the calculated curves show slightly more variations in band speed over the course of propagation under each impact velocity, the calculated average speeds match the average speeds measured in experiments. Also, both the calculated curves and the measured curves show the same dependence on impact velocity. Furthermore, the calculated and the measured curves clearly demonstrate that the duration of shear band propagation is between approximately 20 and $60 \mu\text{s}$ after impact, consistent with the loading changes seen through the contours of the stress components in Figs 2 and 3.

A strong dependence of shear band speed on impact velocity is observed experimentally in Part I of this investigation. Such a strong dependence on loading rate is also predicted by the numerical simulations. The measured and calculated average shear band speeds at different impact velocities are compared in Fig. 11. Reasonable agreement is seen between the measured and computed results. The calculations do show a tendency for the band speed to saturate at high impact velocities. Theoretically, the limiting shear band speed may be a significant fraction of the shear wave speed of the material. Because of the lack of data on material response at very high strain rates and at large strains [such as the details of the behavior which (6) describes], realistic predictions of the limiting speed are not possible at this time. However, the results in Fig. 11 indicate it may well be on the order of 2000 ms^{-1} or higher for C-300 steel. The strong dependence of shear band speed on impact velocity at lower impact velocities and the tendency to saturate at higher impact velocities observed in the

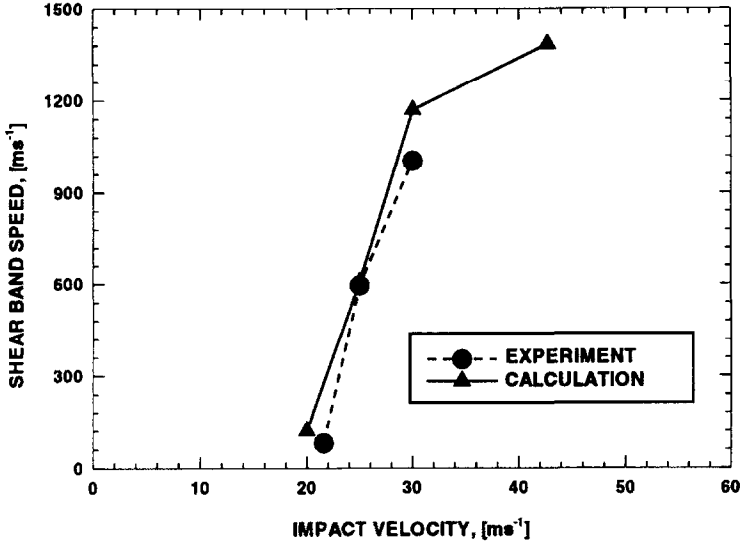


Fig. 11. Comparison of measured and calculated shear band speeds.

experimental and numerical studies here have also been predicted by the boundary layer solution of Gioia and Ortiz (1996). Indeed, consistent with the analysis, the shear band speed obtained here is orders of magnitude higher than the impact velocity. The consistency between the experimental, numerical and analytical results also lends credence to the numerical model presented in this paper.

4.5. Shear band toughness issues

There is a need to characterize material resistance to the initiation and propagation of shear bands. The concept of a shear band toughness was recently proposed by Grady (1992). A realistic understanding of the issue calls for the study of the energy required for band initiation and propagation. The generalized path-independent J -integral for dynamic conditions (Moran and Shih, 1987a, b) is used in the analysis here. This generalized J -integral is given by

$$J = \int_{\Gamma} \left[\left(\int_0^t \tau \cdot d\mathbf{E} + \frac{1}{2} \rho \dot{\mathbf{u}} \cdot \dot{\mathbf{u}} \right) dx_2 - \mathbf{t} \cdot \frac{\partial \mathbf{u}}{\partial x_1} ds \right] + \int_A \left[\alpha (\boldsymbol{\tau} \cdot \mathbf{I}) \frac{\partial T}{\partial x_1} + \rho \ddot{\mathbf{u}} \cdot \frac{\partial \mathbf{u}}{\partial x_1} - \rho \dot{\mathbf{u}} \cdot \frac{\partial \dot{\mathbf{u}}}{\partial x_1} \right] dA, \quad (10)$$

where A is the area inside contour Γ , x_1 and x_2 are Cartesian coordinates in the reference configuration. A series of 10 contours of different sizes emanating from the notch surfaces are used in the analysis. As expected, the calculated J values for these contours remain the same until they are intercepted by the shear band tip. This interception corresponds to the time when the failure criterion of (5) is met at a point on a contour intercepted by the shear band path. The J values for contours that have

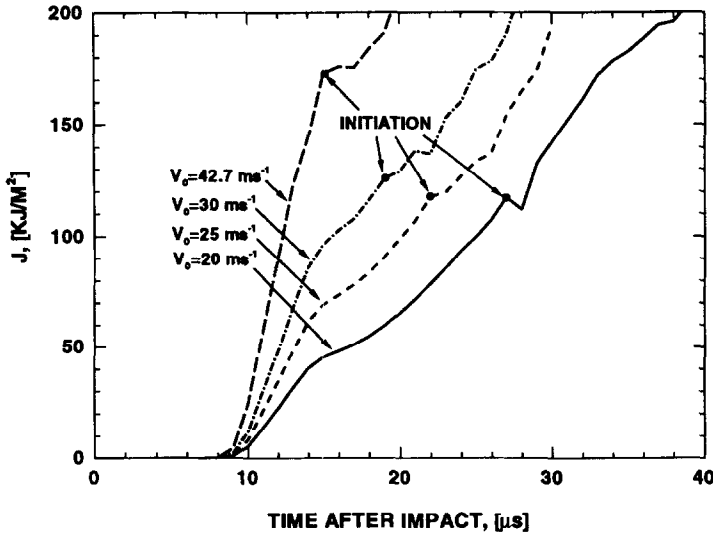


Fig. 12. Time histories of J -integral at different impact velocities.

been intercepted by the shear band deviate from the J value for those contours not yet intercepted. In addition, they differ from each other. These values after interception are not used in the current analysis.

Figure 12 shows the time histories of J for four impact velocities. Since attention is focused on initiation and J is path independent up to the time when a contour is intercepted by the shear band, only the result for the contour closest to the initial notch tip is plotted. For each impact velocity, J increases monotonically before shear band initiation. Higher impact velocities correspond to higher values of J at any given instant. The J values at initiation and the times of initiation for different impact velocities are shown in Fig. 13. First, it is noted that higher impact velocities shorten the time to initiation after impact. At low impact velocities, the value of J at initiation (J_{init}) increases very slowly with impact velocity. At higher impact velocities, J_{init} increases more rapidly. This behavior is analogous to experimental observations of the effect of loading rate on the dynamic fracture toughness of mode-I cracks in metals [see Chapter 8, Freund (1990)].

After shear band initiation, both the shear band speed and J change with time. Since the size of the area with large plastic deformation is relatively small (small scale yielding), J can be regarded as a measure of the driving force for shear band propagation. In Fig. 14, the instantaneous J value is plotted as a function of instantaneous shear band speed for the four impact velocities shown in Fig. 12. The values of J plotted here are for the contour that is farthest from the notch tip, before it is intercepted by the shear band. Therefore, path independence is maintained for the data used. Although the data show a certain amount of scatter, a universal trend of increasing J with increasing shear band speed is observed. It should be noted that the data forming this universal curve correspond to four calculations which involve drastically different shear band speed histories. This may point to the existence of a material-dependent relation between driving force (J) and instantaneous shear band

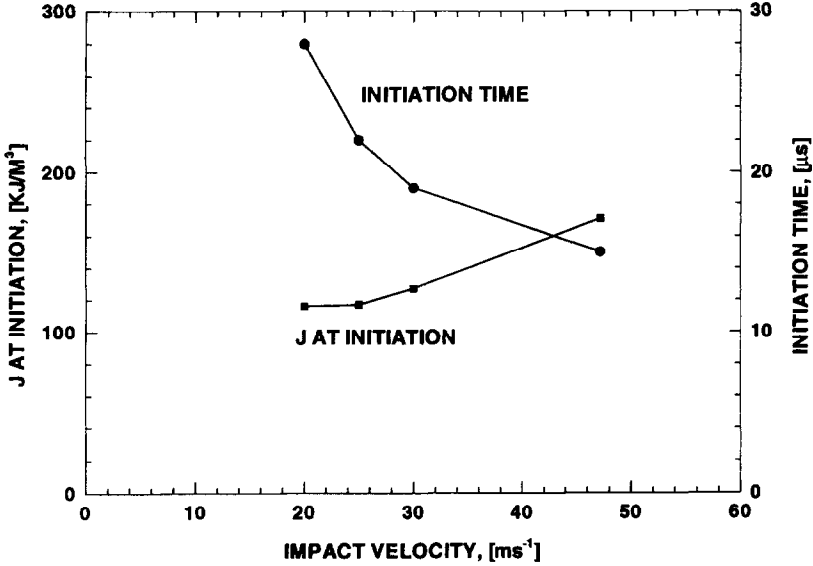


Fig. 13. *J*-integral at time of band initiation.

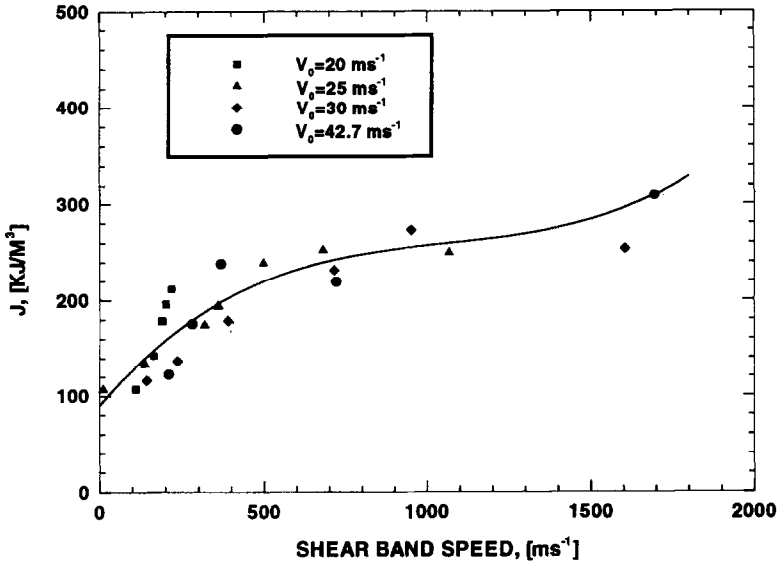


Fig. 14. *J*-integral as a function of shear band initiation at different impact velocities.

speed. Beyond a shear band speed of approximately 500 ms^{-1} the driving force (*J*) appears to reach a saturation value equal to approximately 250 KJ m^{-3} . The results presented in Figs 12–14 are only an initial attempt to approach the issue of shear band toughness by suggesting a possible correlation between a measure of the driving force and shear band propagation speed. Further analyses are certainly needed in

order to achieve a better understanding of material resistance to the initiation and propagation of shear bands.

4.6. Energy evolutions

In addition to the field quantities, energy consumptions provide another perspective on the coupled thermo-mechanical process of shear band propagation.

The principle of virtual work (1) can be written as

$$\int_S \mathbf{f} \cdot \dot{\mathbf{u}} dS = \int_V \boldsymbol{\tau} \cdot \mathbf{D} dV + \frac{d}{dt} \int_V \frac{1}{2} \rho \dot{\mathbf{u}} \cdot \dot{\mathbf{u}} dV. \quad (11)$$

This identity specifies the balance between the rate at which mechanical work is done through the specimen boundary, the stress power and the rate of change of kinetic energy in the specimen. The stress power consists of an elastic part, a plastic part and a thermal part, i.e.

$$\int_V \boldsymbol{\tau} \cdot \mathbf{D} dV = \int_V \boldsymbol{\tau} \cdot \mathbf{D}^e dV + \int_V \boldsymbol{\tau} \cdot \mathbf{D}^p dV + \int_V \boldsymbol{\tau} \cdot \mathbf{D}^t dV. \quad (12)$$

Integrating (10) in time, one obtains

$$\int_0^t \int_S \mathbf{f} \cdot \dot{\mathbf{u}} dS dt = \int_0^t \int_V \boldsymbol{\tau} \cdot \mathbf{D} dV dt + \int_V \frac{1}{2} \rho \dot{\mathbf{u}} \cdot \dot{\mathbf{u}} dV, \quad (13)$$

where $\mathcal{P}(t) = \int_0^t \int_S \mathbf{f} \cdot \dot{\mathbf{u}} dS dt$ is the accumulated boundary work at time t , $\mathcal{K}(t) = \int_V \frac{1}{2} \rho \dot{\mathbf{u}} \cdot \dot{\mathbf{u}} dV$ is the total kinetic energy in the specimen and $\mathcal{W}(t) = \int_0^t \int_V \boldsymbol{\tau} \cdot \mathbf{D} dV dt$ is the accumulated stress work. The elastic, plastic and thermal parts of \mathcal{W} are denoted by \mathcal{W}^e , \mathcal{W}^p and \mathcal{W}^t , respectively.

Figure 15 shows the evolutions of boundary work \mathcal{P} , stress work \mathcal{W} and kinetic energy \mathcal{K} . The three parts of \mathcal{W} are also shown. As in Figs 2 and 3, the impact

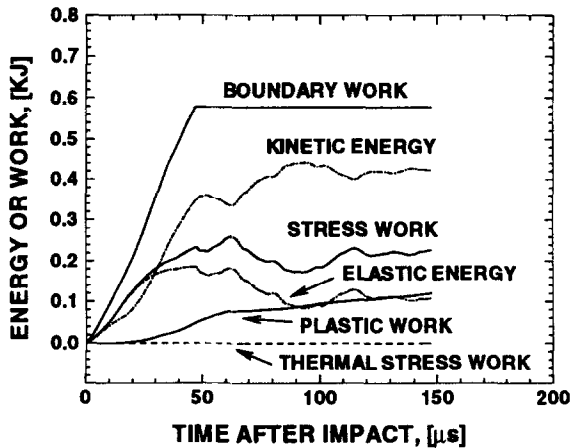


Fig. 15. Work and energy evolutions, $V_0 = 25 \text{ ms}^{-1}$.

velocity is 25 ms^{-1} . Boundary work \mathcal{P} , which is the total work imparted to the specimen by the projectile through the impact face, increases nearly linearly for up to $47 \mu\text{s}$ when the velocity boundary condition is imposed and remains constant afterwards when projectile–specimen separation is assumed. Initially, the stress work \mathcal{W} increases faster than the kinetic energy \mathcal{K} , indicating that more energy is stored in the specimen as elastic energy since plastic work is very small in this part of the deformation. As the deformation continues, the rate of change of the kinetic energy increases while the stress work rate decreases. By approximately $30 \mu\text{s}$, \mathcal{K} exceeds \mathcal{W} , signifying that a major part of the boundary work translates into kinetic energy. The changes in \mathcal{K} and \mathcal{W} are always opposite in sign when no additional work is being imparted into the specimen through the boundary, indicating the interchange of kinetic and elastic energies in the specimen. The plastic work is smaller relative to the elastic and kinetic energies, reflecting the relatively small size of the area in the specimen that undergoes plastic deformation. Almost all of the stress work is stored as elastic energy for up to $18 \mu\text{s}$ after impact when significant plastic deformation commences in the notch tip region. The plastic work \mathcal{W}^p increases steadily after the onset of significant plastic deformation near the notch tip and throughout the duration of shear band propagation. The rate of plastic work decreases significantly with the arrest of the shear band at approximately $60\text{--}62 \mu\text{s}$. It remains small thereafter since subsequent deformation involves much less dissipation. Clearly, there is a correlation between the evolution of loading conditions as shown in Figs 2 and 3 and work–energy changes shown in Fig. 15. Higher rates of plastic work accompany the initiation and propagation of the shear band. The plot also show that thermal stress work \mathcal{W}^t remains essentially zero throughout the deformation.

5. CONCLUSIONS

Finite element simulations are conducted to investigate the initiation and propagation of shear bands and the transition of failure mode from shear banding to fracture in prenotched plates impacted asymmetrically. In the simulations, shear band development is assumed to be controlled by a rate-dependent critical strain criterion and the initiation of fracture is assumed to be controlled by a maximum tensile stress criterion. The simulations demonstrate the evolution of the loading characteristics in the tip region of the shear band. The initiation and propagation of the shear band are driven by the in-plane shear loading generated by the asymmetric impact. The shear band arrests when this loading condition ceases to exist. Further evolution of the stress waves inside the specimen subjects the arrested shear band to a mixed-mode loading. This mode of loading causes a crack to initiate from the tip of the notch and propagate in a direction approximately 30° away from the direction of shear band propagation, consistent with the experimental observation of Part I.

The simulations give visual demonstrations of shear band propagation and predict average speeds of shear band propagation that agree with experimental observations. Furthermore, the calculated shear band speeds show the same dependence on impact velocity as that measured in experiments. There is an active plastic zone in front of the tip of the propagating shear bands inside which plastic deformation occurs. The

size of this zone is approximately 9 mm in the direction of shear band propagation and does not change significantly with impact velocity. The shear stress is uniform inside this zone except near the immediate band tip where higher rates of strain exist. This zone remains self-similar throughout propagation. The shear band behind the propagating tip is well-defined and exhibits highly localized deformation and intense heating. The calculations confirm the experimental observation that plastic dissipation continues behind the propagating tip of the shear band. As a result of this continued dissipation, temperatures inside the band increase to significant fractions of the melting point of the material. Temperature rises are smaller in the plastic zone compared with those inside the well-developed shear band behind the running tip. Unlike in the case of one-dimensional shear bands, deformation and temperature are not uniform along the line of propagating shear bands. Good agreements are found between calculated temperature-rise profiles and those measured in experiments.

ACKNOWLEDGEMENTS

The authors gratefully acknowledge support from the Army Research Office through grant No. DAAH 04-93-G0037 under Dr K. Iyer. We are also grateful to Dr Y. Rajapakse for support from the Office of Naval Research through grant No. N00014-90-J-1340. The computations were carried out on a Cray C98 computer at the Goddard Space Center and a Cray Y-MP2E/232 computer at the Jet Propulsion Laboratory. We would also like to thank Professor M. Ortiz of Caltech for a series of helpful discussions that enhanced our understanding of this problem.

REFERENCES

- Belytschko, T., Chiapetta, R. L. and Bartel, H. D. (1976) Efficient large scale non-linear transient analysis by finite elements. *Int. J. Numer. Meth. Engng* **10**, 579–596.
- Freund, L. B. (1990) *Dynamic Fracture Mechanics*. Cambridge University Press.
- Gioia, G. and Ortiz, M. (1996) The two-dimensional structure of dynamic shear bands in thermoviscoplastic solids *J. Mech. Phys. Solids* **44**, 251–292.
- Grady, D. E. (1992) Properties of an adiabatic shear-band process zone. *J. Mech. Phys. Solids* **40**, 1197–1215.
- Grady, D. E. (1994) Dissipation in adiabatic shear-bands. *Mech. Mater.* **17**, 289–293.
- Hanchak, S. J., Altman, B. S. and Forrestal, M. J. (1993) Perforation of HY-100 steel plates with long rod projectiles. *Proc. 13th Army Symposium on Solid Mechanics*, pp. 247–256, Plymouth, MA.
- Kalthoff, J. F. (1987) Shadow optical analysis of dynamic shear fracture. *SPIE, Photomechanics and Speckle Metrology* **814**, 531–538.
- Kalthoff, J. F. and Wrinkler, S. (1987) Failure mode transition at high rates of shear loading. *Impact Loading and Dynamic Behavior of Materials* (eds C. Y. Chiem, H.-D. Kunze and L. W. Meyer), Vol. 1, pp. 185–195.
- Krieg, R. D. and Key, S. W. (1973) Transient shell response by numerical time integration. *Int. J. Numer. Meth. Engng* **7**, 273–286.
- Lee, Y. J. and Freund, L. B. (1990) Fracture initiation due to asymmetric impact loading of an edge cracked plate. *Trans. ASME* **57**, 104–111.
- LeMonds, J. and Needleman, A. (1986) Finite element analyses of shear localization in rate and temperature dependent solids. *Mech. Mater.* **5**, 339–361.

- Magness, L. S. (1994) High strain rate deformation behaviors of kinetic energy penetrator materials during ballistic impact. *Mech. Mater.* **17**, 147–154.
- Moran, B. and Shih, C. F. (1987a) Crack tip and associated domain integrals from momentum and energy balance. *Engng Fract. Mech.* **27**, 615–642.
- Moran, B. and Shih, C. F. (1987b) A general treatment of crack tip contour integrals. *Int. J. Fract.* **35**, 295–310.
- Mason, J. J., Rosakis, A. J. and Ravichandran, G. (1994a) Full field measurements of the dynamic deformation field around a growing adiabatic shear band at the tip of a dynamically loaded crack or notch. *J. Mech. Phys. Solids* **42**, 1679–1697.
- Mason, J. J., Rosakis, A. J. and Ravichandran, G. (1994b) On the strain and strain-rate dependence of the fraction of plastic work converted to heat: An experimental study using high speed infrared detectors and the Kolsky Bar. *Mech. Mater.* **17**, 135–145.
- Needleman, A. (1989) Dynamic shear band development in plane strain. *J. Appl. Mech.* **56**, 1–9.
- Needleman, A. and Tvergaard, V. (1994) Analysis of dynamic, ductile crack growth in a double edge cracked specimen. *Int. J. Frac.* **49**, 41–67.
- Needleman, A. and Tvergaard, V. (1994) Analysis of brittle-ductile transition under dynamic shear loading. Symposium on the Dynamic Failure Mechanics of Modern Materials, Caltech, Pasadena, CA, 3–5 February 1994
- Nesterenko, V. F., Meyers, M. A., Chen, H. C. and LaSalvia, J. C. (1994) Controlled high-rate localized shear in porous reactive media, Institute for Mechanics and Materials Report No. 94–11, UCSD.
- Povirk, G. L., Nutt, S. R. and Needleman, A. (1993). Continuum modelling of residual stress in metal-matrix composites. *Residual Stresses in Composites: Measurement, Modelling and Effect on Thermo-Mechanical Properties*, to be published,
- Zehnder, A. T. and Rosakis, A. J. (1992) Temperature rise at the tip of dynamically propagating cracks: measurements using high-speed infrared detectors. *Experimental Techniques in Fracture* (ed. J. S. Epstein), Ch. 3, pp. 125–169. VCH Publishers.
- Zhou, M., Needleman, A. and Clifton, R. J. (1994) Finite element simulations of dynamic shear localization in plate impact. *J. Mech. Phys. Solids* **42**, 423–458.
- Zhou, M., Rosakis, A. J. and Ravichandran, G. J. (1996) Dynamically propagating shear bands in prenotched plates—I. Experimental investigations of temperature signatures and propagation speed. *J. Mech. Phys. Solids* **44**, 981–1006.